Zn/Co-ZIF reinforced Sugarcane Bagasse Aerogel for Highly Efficient Catalytic Activation of Peroxymonosulfate

Yongxin Lei[a], Wen Sun[a], Santosh K. Tiwari[a], Kunyapat Thummavichai[b], Oluwafunmilola Ola[c], Xupeng Qin[a], Zhiyuan Ma[a], Nannan Wang[a]* and Yanqiu Zhu[a]

[a] Guangxi Institute Fullerene Technology (GIFT), Key Laboratory of New Processing Technology for Nonferrous Metals and Materials, Ministry of Education, School of Resources, Environment and Materials, Guangxi University, Nanning, 530004, China

[b] College of Engineering, Mathematics and Physical Sciences, University of Exeter, Exeter, EX4 4QF, United Kingdom

[c] Advanced Materials Group, Faculty of Engineering, The University of Nottingham, Nottingham, NG7 2RD, United Kingdom

Abstract:

Sugarcane bagasse is the main solid waste of sugar extraction industry. However, there are less eco-friendly treatment methods for this kind of waste material. Most of them have been burned and this is a challenge for effective utilization of sugarcane. Herein, Zn/Co-ZIF nanoparticles are loaded onto the aerogel obtained from bagasse cellulose by doping method to form pomegranate-like structure products, i.e., Zn/Co-ZIF@GEL. By simulating the pomegranate-biomimetic structure, the leaching of cobalt ions is suppressed and enhanced its catalytic activity. Also, Zn/Co-ZIF@GEL behaves outstanding peroxymonosulfate (PMS) activation reactivity to degrade Rhodamine B (RhB) with achieving 100% removal rate in 30 min with enhanced water stability. The outer wrapping of nanoparticles by aerogel exhibits excellent reusability and the removal rate remains above 92% after 4 cycles. X-ray photoelectron spectroscopy (XPS) verifies the electron transfer between the heterostructures of Zn and Co could ensure the catalyst continues to complete the redox cycle with synergistic effect. Electron paramagnetic resonance (EPR) further investigates the non-radical singlet oxygen is the predominant degradation pathway of RhB. This work provides a new strategy for improved bagasse derivate ZIF catalytic application.

Keywords:

Bagasse cellulose aerogel, Zeolitic imidazolate frameworks, Zn doped, Peroxymonosulfate (PMS) Oxidation, Water stability

1.Introduction

The conversion of biomass materials into green materials is an environmental-friendly option, showing especially candidate prospects for the development of circular bioeconomy [1, 2]. Sugarcane is a widely planted crop and mostly used in sugar industry. The global production of its by-product, bagasse, is as high as 2.79 metric tons in recent year [3]. Owing to technical limitations, labor and transportation costs, bagasse is mostly landfilled or incinerated in situ, which causes great pollution to the environment. However, bagasse is rich in natural resources, renewable, biodegradable and non-polluting to the environment, due to which it is a green by-product of sustainable development. Over the past years, bagasse has been used in films and coatings, [1] glass ceramic materials [4], geopolymers [5], ceramic raw materials [6], synthetic zeolites [7] and so on [8, 9]. Unfortunately, owing to the limitation of technology and cost constraints, the above-mentioned applications of bagasse have not been widely used. In recent years, metal-organic framework/cellulose composite materials have attracted more attention. Zhu et al. [10] modified cellulose with aldehyde-hydrazine and loaded with four different MOFs, including HKUST-1, ZIF-8, ZIF-67 and MIL-100, which could effectively remove Rhodamine B, Cr (VI) ions and benzotriazole. Yang et al. [11] used three-dimensional sodium carboxymethyl cellulose aerogel as the substrate of Ni/Co-MOF, and the composite aerogel could effectively remove tetracycline hydrochloride in 5 min with the removal efficiency of 80%. Because of the super toughness of cellulose, it can be used as a mechanical support to prepare composite materials with flexibility, formability and graded porosity [12, 13]. As a kind of abundant cellulose material which can be extracted from plants, bagasse cellulose has great potential in practical applications. So that making full use of bagasse resources will have a long-term and profound impact on waste treatment and environmental protection.

At present, the problem of water pollution has become a worldwide environmental governance problem. Organic pollutants such as drugs [14], personal care products [15], dyes [16], etc., are difficult to treat with conventional water treatment processes for

their complex chemical structures, causing serious water environmental pollution problems.. In addition, advanced oxidation process (AOPs) is a promising, efficient and high-speed water treatment method that thoroughly oxidizes recalcitrant organic pollutants in wastewater [17, 18]. Li et al. successfully constructed three isoreticular porous 1D rod-based Ti-MOFs denoted as ZSTU-1, ZSTU-2 and ZSTU-3 for highly effective visible-light photocatalysts for H_2 [19]. Zhou et al. reported on the use of light-driven perylene diimide-based catalysts for the degradation of trace organic pollutants present in the aqueous environment [20]. He et al. preparation Mn and O co-doped polymeric carbon nitride with electronic structure modulate by Mn and O co-dopants for enrofloxacin removal [21]. The AOPs based on peroxymonosulfate (PMS) has shown great potential in the removal of organic pollutants. As a widely used oxidant, PMS can be activated by a variety of transition metal ions (such as Mn^{2+}, Co^{2+}, Ni^{2+}, Fe^{2+}, etc.), among which the Co^{2+}/PMS system has the highest efficiency [22, 23]. However, the transition metal Co^{2+} is easy to dissolve in the reaction system, causing the problem of secondary pollution [24].

Metal-organic frameworks (MOFs), also known as porous coordination polymers. Due to the unique porous structure, ultra-high specific surface area and strong adsorption capacity, MOFs attract wide attention for its potential applications in the fields of separation, chemical sensing, ion exchange, energy storage and transformation, drug delivery and catalysis [25-32]. Zeolitic imidazolate frameworks (ZIFs), the subclass of MOFs, are as porous crystalline solid composed of tetrahedral divalent metal ions (Zn^{2+}, Co^{2+}) connect with imidazole derivatives by coordination bonds [33, 34]. Since cobalt has been proven to be the most common and effective catalyst for PMS, cobalt-based MOFs and the derivative materials, e.g., ZIF-67, attract much attention in water treatment applications[35, 36]. Lin et al. [23] used ZIF-67 as a heterogeneous catalyst to activate PMS to degrade Rhodamine B, and the degradation equilibrium could be achieved within one hour at room temperature. Zhang et al. [37] prepared yolk-shell Co_3O_4/C@SiO_2 nanoreactors and ZIF-67 was used as the precursors for carbon and cobalt species, it could effectively degraded 90.1% of Bisphenol A (BPA) in the presence of PMS. However, because of its powder

characteristics, MOFs are difficult to separate from water and recover from a large number of reaction solutions, which hinders their application in water pollution treatment [38]. Therefore, it is essential to reinforce the stability and recoverability of MOFs in water. MOFs-based hydrogels and aerogels provide processability, better stability and easier handling. Ren et al. used in situ synthesis to load ZIF-8 and ZIF-12 onto cellulose aerogels and successfully activated PMS [39]. We propose that such a green strategy to prepare aerogels from biomass waste for loading MOFs particles is highly desirable, which would further boost the stability of MOFs and even provide opportunities to expand the potential applications of biomass materials.

In this experiment, we sought to construct cellulose aerogel was made from bagasse as raw material. and Zn/Co-ZIF@GEL composite aerogel was prepared by doping method which was used as heterogeneous catalyst to catalyze potassium peroxymonosulfate oxidant to degrade RhB. Catalyst performance was evaluated under different reaction conditions (Zn/Co ratios, catalyst dosage, initial pH, PMS dosage and initial concentration of RhB). On one hand, cellulose aerogels served as the skeleton of Zn/Co-ZIF to wrap nanoparticles that could improve the stability in solution, and simplify the catalyst recovery method without affecting the degradation performance. On the other hand， the doping of Zn^{2+} significantly reduced the dissolution amount of transition metal cobalt which could solve the problem of secondary pollution and avoid the reduce of recycle performance. In addition, the catalytic degradation mechanism and pathways of RhB were investigated by XPS, radical-quenching tests and EPR experiments. In this paper, agricultural waste bagasse was transformed into a carrier for water pollution treatment and synthetic composite aerogel was a kind of green and stable long-term ideal material for removing organic pollutants from wastewater.

2. Experimental

2.1. Chemical Reagents

Cobalt nitrate hexahydrate ($Co(NO_3)_2 \cdot 6H_2O$, 99%), zinc nitrate hexahydrate ($Zn(NO_3)_2 \cdot 6H_2O$, 99%), 2-methylimidazole (2-MeIM), anhydrous methanol (MeOH), sodium hydroxide (NaOH), urea, N,N′-methylenebisacrylamide (MBA), *tert*-butanol (TBA), sodium thiosulfate ($Na_2S_2O_3 \cdot 5H_2O$), were purchased from Sinopharm Chemical Reagent Co., Ltd.; Rhodamine B (RhB), 2,2,6,6-Tetramethyl-4-piperidone(TEMP), 5,5-dimethyl-1-pyrroline N-oxide (DMPO), and potassium peroxymonosulfate (PMS, $KHSO_5 \cdot 0.5KHSO_4 \cdot 0.5K_2SO_4$) were obtained from Macklin. All the materials used in this study were of analytical grade and used as received without further purification. Deionized water was applied in all the experiments.

2.2. Synthesis of Catalysts

2.2.1. Extraction of Cellulose from Sugarcane Bagasse

Cellulose was obtained from sugarcane bagasse through a facile alkaline extraction process. Firstly, the bagasse was grounded into small size, then washed with deionized water and ethanol for several times, collected by filtration and dried at -12 ℃ overnight to obtained the bagasse powder. Secondly, the bagasse powder was dewaxed in the mixture of toluene-ethanol (2:1 v/v) using a Soxhlet extractor for 6 hours. Thirdly, the pretreated bagasse (20 g) was soaked in NaOH solution (600 mL, 4 wt%) and stirred at 80°C for 4 hours. Then, the resulting sugarcane cellulose was obtained after washed with deionized water and ethanol for several times to remove the residual impurities. Subsequently, a certain amount of cellulose was placed into $NaClO_2$ solution (4 wt%, pH = 4, adjusted with glacial acetic acid), and stirred at 80 ℃ for 4 hours until white cellulose suspension was obtained, which was washed with deionized water to neutral. Finally, after dried in vacuum at 60°C for 12 hours, the purified sugarcane cellulose was obtained.

2.2.2 Synthesis of Cellulose Aerogel

First, the NaOH/Urea/H_2O cellulose mixture was prepared with a mass ratio of 7: 12: 81, stored them in the refrigerator, and frozen at -12 ℃ for 12 hours. The 4 g of

bagasse fibers were added to 96 g configured cellulose dissolving solution, stirred, and when the solution became clearer and more transparent, to which was added 0.8 g MBA. The solution was then poured into a well plate to stand until the liquid phase was converted to gel state. The cellulose hydrogel was peeled from the well plate and washed repeatedly with deionized water. Finally, freeze-dried to obtain cellulose aerogel. By adjusting the amount of bagasse cellulose added, different concentrations of bagasse cellulose aerogels (2.5 wt%, 3 wt%, 4 wt%) were obtained.

2.2.3 Synthesis of Zn doped Co-ZIF (Zn/Co-ZIF)

The 3 mmol of cobalt nitrate hexahydrate and zinc nitrate hexahydrate was dissolved in 90 ml of methanol, 48 mmol of 2-methylimidazole were dissolved in 90 ml of methanol. After stirring for 5 minutes at room temperature, the methanol solution of mixed metal ions was poured into the 2-methylimidazole solution, and the mixture was stirred and then left to stand. The obtained purple suspension was washed with methanol several times, and the sample was collected by centrifugation. By adjusting the ratio of transition metal cobalt and zinc (Co: Zn = 5: 5, 6: 4, 7: 3, 8: 2, 9: 1) to prepare ZIFs materials with different doping ratios.

2.2.4. Synthesis of Zn doped Co-ZIF@Aerogel (Zn/Co-ZIF@GEL)

First, 4 g of purified bagasse cellulose was added to 96 g of cellulose solution and placed in a mechanical agitator for intense stirring. 1 g of Zn/Co-ZIF was added to the solution and stirred evenly. 0.3 g of MBA was added and continued to be stirred and ultrasonic. The solution is then poured into the orifice plate to stand and washed with deionized water. Finally, the Zn/Co-ZIF@GEL composite aerogel was obtained by freeze-drying. The schematic of the Pomegranate-like Zn/Co-ZIF@GEL synthesis process is illustrated in Fig. 1.

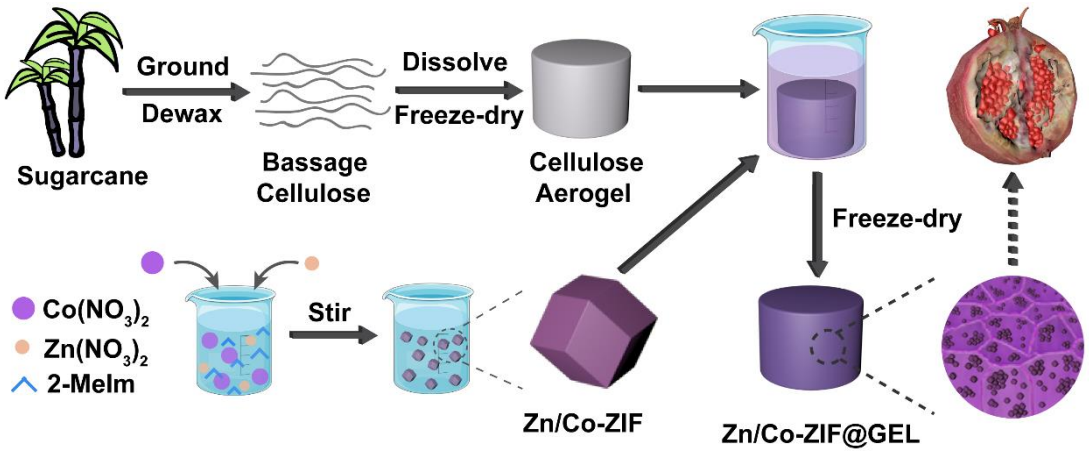

Fig. 1. The schematic of the Zn/Co-ZIF@GEL preparation process.

2.3. Material Characterizations

The composition and water stability of the cellulose were analyzed by X-ray diffraction (XRD, Bruker D8, Germany) with Cu Kα radiation (100 mA, 40 kV) at a scanning rate of 5° min^{-1}. The surface morphology of MOFs on aerogels was studied by field emission scanning electron microscopy (FESEM, Hitachi S-4800, Japan) and high-resolution transmission electron microscopy (HRTEM, JEM-2010, Japan). The mixed cellulose aerogels were characterized by thermogravimetric analysis (TGA, TG 209F1, Germany). The heating rate was 20℃ min^{-1} and the temperature was 30 ~ 800℃ in nitrogen atmosphere. Free radicals in the system were detected by electron paramagnetic resonance (EPR, Bruker A300, Germany) with a modulation amplitude of 3G, microwave power of 20.00 mW, microwave frequency of 9.79 GHz, and modulation frequency of 100 kHz. The elemental composition and valence states of the material were analyzed by X-ray photoelectron spectroscopy (XPS, Axis Ultra DLD, England). Al Kα was used as the radiation source. The measurement range was from 0 eV to 1380 eV. After the degradation experiment, the cobalt element was analyzed by inductively coupled plasma atomic emission spectrometry (ICP-MS, ICPS-7510, Japan).

2.4. Catalytic Activity Measurements

The degradation experiments were carried out in a 250 ml beaker at 25 ℃. The RhB stock solution was dissolved in deionized water and stirred for 12 hours to prepare a RhB solution with a concentration of 50 mg/L, with an initial pH of 6.8. In typical

procedure, a certain amount of catalyst was added to the RhB solution and stirred for 5 minutes to completely disperse the catalyst. Subsequently, a predetermined dose of PMS was added. Drew out the reaction solution (1 mL) and injected it into the $Na_2S_2O_3$ solution (50 μL) at regular intervals to scavenge free radicals and prevent further reactions. The catalytic efficiency is Ct/Co (Ct: concentration of the reaction RhB, Co: RhB initial concentration), and the concentration of RhB was measured at 554 nm using UV spectrophotometer. Measured by the composite aerogels and bagasse cellulose aerogel density, calculated as the following equation aerogel composite load:

$$\text{Loading rate} = (\rho_c - \rho_a) / \rho_c$$

ρ_c represents the density of the mixed cellulose aerogel, and ρ_a represents the density of the cellulose aerogel. The calculated load rate of the mixed aerogel was 48 ± 1.8%, and the calculated load rate of the composite aerogel was 31 ± 1.2 wt%.

3. Results and Discussion

3.1. Function of Zn doping in enhancing hydrostability of Co-ZIF

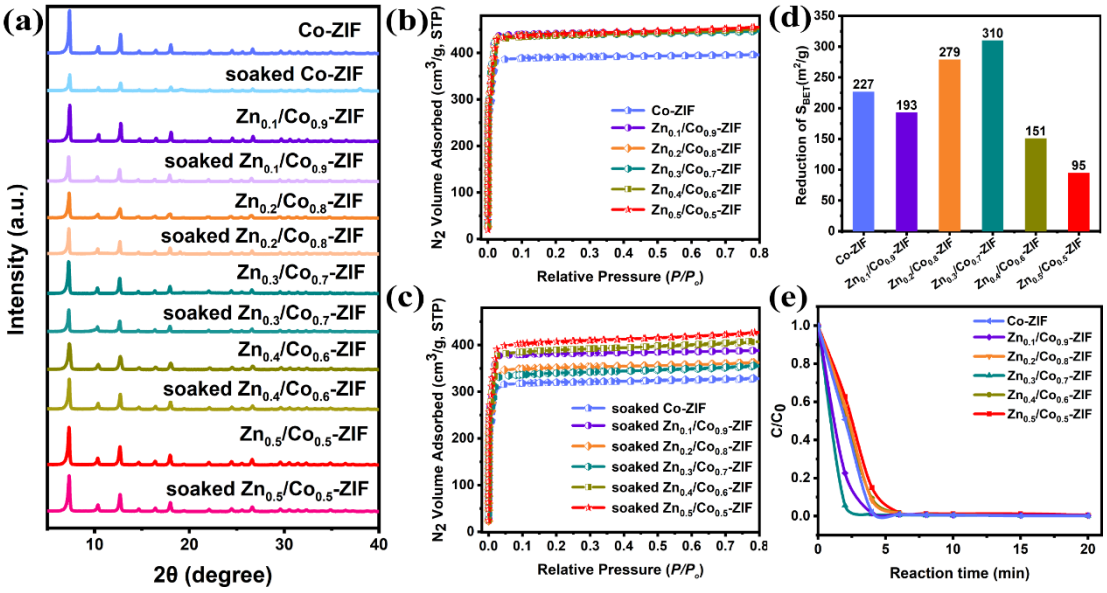

Fig. 2. (a) XRD patterns of Zn_x/Co_{1-x}-ZIF before and after soaking in water for 12 h, (b)(c) N_2 adsorption-desorption isotherm curves, (d) BET surface area data of Co-ZIF and Zn_x/Co_{1-x}-ZIF, (e) degradation efficiency diagram of RhB by Zn/Co-ZIF with different Zn/Co ratios.

Considering the Co-ZIF was moisture-sensitive and suffered from structure collapse due to the attack of water molecules, Zn doping was proposed to enhance the structural stability of Co-ZIF after soaking in water [40]. The crystal and pore structure were two important structural features among ZIFs and were separately confirmed by XRD and N_2 adsorption-desorption analyses. Fig. 2a shows the XRD patterns of Co-ZIF and Zn_x/Co_{1-x}-ZIF composites before and after soaking in water. Zn_x/Co_{1-x}-ZIF composites with different Zn doping ratios had the same SOD topology structure as the pure Co-ZIF ~~., indicating that the Zn(II) ions have been successfully doped into the framework and a portion of Co(II) ions has been well substituted in the $[Co_4O]^{6+}$ clusters~~ [41]. According to other reports, all the different Zn/Co ratio of Zn/Co-ZIF were isostructural to Co-ZIF [42], and the result was consistent with reported works. The soaked Co-ZIF showed much weaker peaks than pure Co-ZIF, suggesting that there was some decomposition happened in the framework after soaking. Since Co-N bonds are more

vulnerable to hydrolysis than Zn-N bonds [43]. After doping of Zn, the change in the peaks of Zn_x/Co_{1-x}-ZIF before and after soaking became smaller than that of Co-ZIF, which means that doping of Zn in the lattice results in different levels of enhancement in the hydrostability of Co-ZIF. Noticeably, the crystallinity and hydrostability of $Zn_{0.5}/Co_{0.5}$-ZIF was superior to the other Zn doped Co-ZIF.

N_2 adsorption-desorption measurements were performed to further explore the pore hydrostability of ZIFs, the surface area and pore-size distribution were analyzed by Brunauer-Emmett-Teller (BET) measurements. Fig. 2b and c shows the N_2 adsorption-desorption isotherms of pure Co-ZIF and five different doping ratios Zn_x/Co_{1-x}-ZIF before and after soaking. As seen in Fig. 2b, all Zn_x/Co_{1-x}-ZIF exhibited similar microporous behavior (Type I isotherms) and almost identical equilibrium N_2 adsorbed volume, which was much higher than that of Co-ZIF. This indicated that the Zn-doping was favorable for improved pore volume in Co-ZIF [32]. After soaking in water, as displayed in Fig. 2c, all samples suffered from different extent of reduction of pore volume after soaking treatment for 12 h. The reduction surface area of Co-ZIF, $Zn_{0.1}/Co_{0.9}$-ZIF, $Zn_{0.2}/Co_{0.8}$-ZIF, $Zn_{0.3}/Co_{0.7}$-ZIF, $Zn_{0.4}/Co_{0.6}$-ZIF and $Zn_{0.5}/Co_{0.5}$-ZIF were calculated to be 227 (22.4), 193 (15.9), 279 (24.9), 310 (28.6), 151 (12.2), and 95 m^2/g (7.3%), respectively. The doping of Zn had significant influence in the enhancement of pore hydrostability for Co-ZIFs except $Zn_{0.2}/Co_{0.8}$-ZIF and $Zn_{0.3}/Co_{0.7}$-ZIF. Noticeably, the $Zn_{0.5}/Co_{0.5}$-ZIF showed the lowest reduction of surface area, suggesting its highest hydrostability to other prepared Zn doped ZIF, which was in good agreement with XRD results. The enhanced hydrostability of Co-ZIFs via Zn doping could be attributed to the enhanced inertness of Zn compared with Co and more stable of $[Zn_x(Co_{4-x})O]^{6+}$ clusters than $[Co_4O]^{6+}$ clusters, which could decrease the hydrolysis vulnerability [29, 44]. Further confirmed that Zn(II) ions have been successfully doped into the framework and a portion of Co(II) ions has been well substituted in the $[Co_4O]^{6+}$ clusters. However, higher doping ratio of Zn may have adverse effect on the catalytic performance of Co-ZIFs due to the inertness of Zn. Among all the samples, considering the $Zn_{0.5}/Co_{0.5}$-ZIF has the highest hydrostability and comparable catalytic activity and

kinetic to Co-ZIF (Fig. 2e), 50% was selected as the optimized doping ratio of Zn for achieving high hydrostability of Co-ZIF based catalysts in the following work.

3.2. Structural characterization of $Zn_{0.5}/Co_{0.5}$-ZIF@GEL

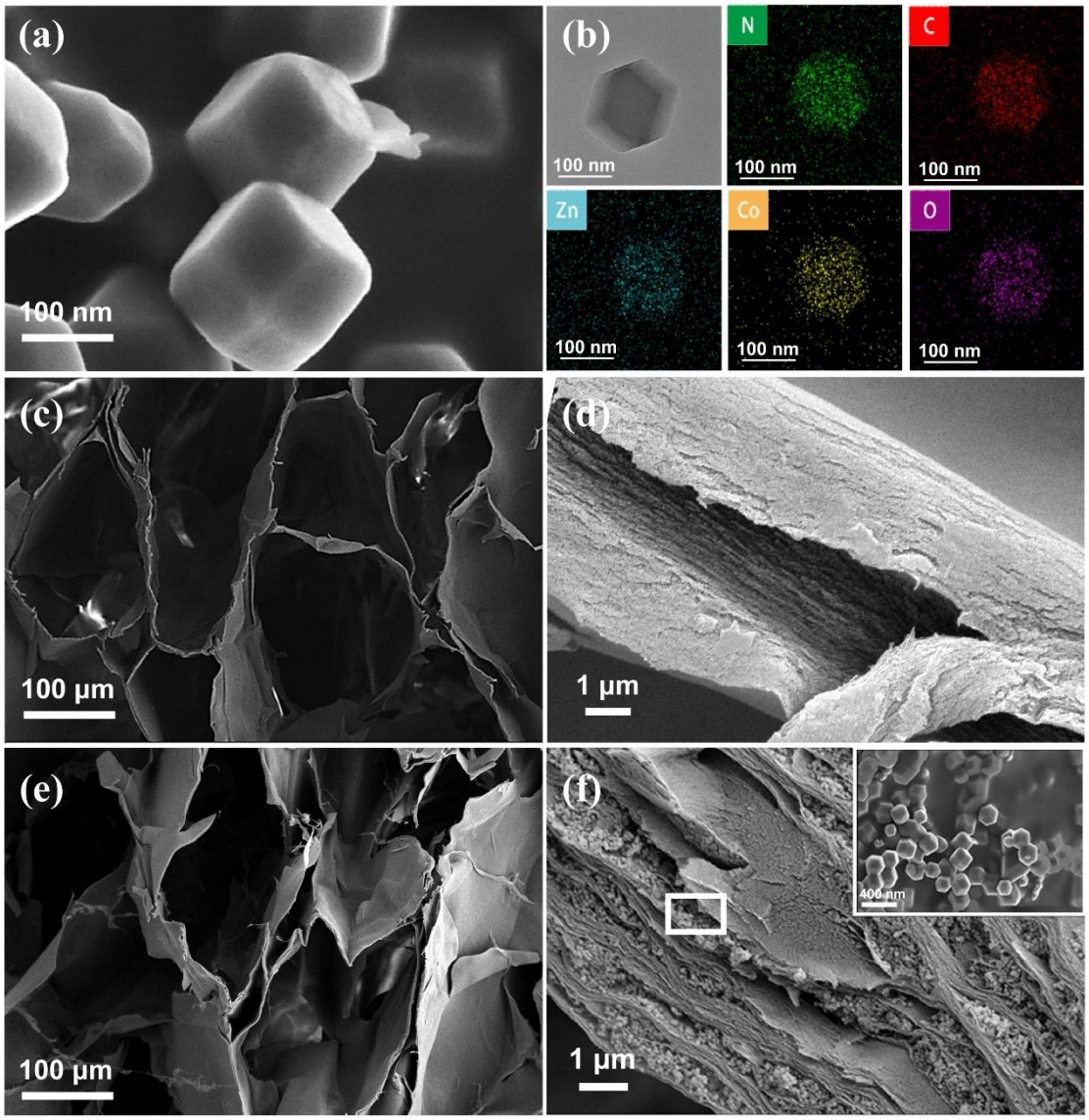

Fig. 3. SEM images of (a) $Zn_{0.5}/Co_{0.5}$-ZIF, (b) HAADF-STEM image and element mapping of $Zn_{0.5}/Co_{0.5}$-ZIF, (c)(d) bagasse cellulose aerogels, (e)(f) $Zn_{0.5}/Co_{0.5}$-ZIF@GEL, the upper right corner is the SEM image of Zn/Co-ZIF loaded on aerogel.

The morphologies and microstructures of GEL, Zn/Co-ZIF and Zn/Co-ZIF@GEL were characterized using both SEM and HRTEM analyses (Fig. 3). Fig. 3a is the SEM image of $Zn_{0.5}/Co_{0.5}$-ZIF. It was a typical rhombohedral dodecahedron crystal

morphology and the grain size was evenly distributed between 250 and 300 nm. This was similar to the image of Co-ZIF (Fig. S1), indicating that the doping of Zn rarely damages the morphology of Co-ZIF. To further research the elemental composition of $Zn_{0.5}/Co_{0.5}$-ZIF@GEL, HAADF-STEM elemental mapping was carried out and the results are shown in Fig. 3b. The distribution of N, C, Zn, Co and O were homogeneous throughout the composite aerogel, reconfirming the successful doping of Zn and assembling of $Zn_{0.5}/Co_{0.5}$-ZIF heterostructure.

As shown in Fig. 3c, bagasse cellulose aerogel has a three-dimensional network structure with large pores (100-300 μm) and honeycomb structures. The solution can pass through the pores in a large amount. Fig. 3d is a partial enlarged view of Fig. 3c. The cross-section of the pore walls of bagasse cellulose aerogel were rough and full of folds, but the pore walls were relatively smooth. It can be seen that $Zn_{0.5}/Co_{0.5}$-ZIF@GEL has the similar morphology and internal structure with GEL (Fig. 3e). The porous structure can expand the diffusion surface area of RhB molecules in the solution and enhance the residence time of RhB molecules when flowing in the channel. After the bagasse cellulose aerogel was compounded with Zn/Co-ZIF, the basic morphology structure of the aerogel remains almost the original state. Fig. 3f is a magnified image of $Zn_{0.5}/Co_{0.5}$-ZIF@GEL. It can be observed that the thickness of the pore walls had increased several times, and the inside of the cellulose pore walls were divided into many layers, and dense Zn/Co-ZIF nanoparticles were inserted between the layers to form a sandwich structure. It was indicated that Zn/Co-ZIF@GEL has a pomegranate-like morphology with GEL as peel and Zn/Co-ZIF nanoparticles as pomegranate seeds, so that nanoparticles could be coated with aerogel and maintain its stability in reaction solution.

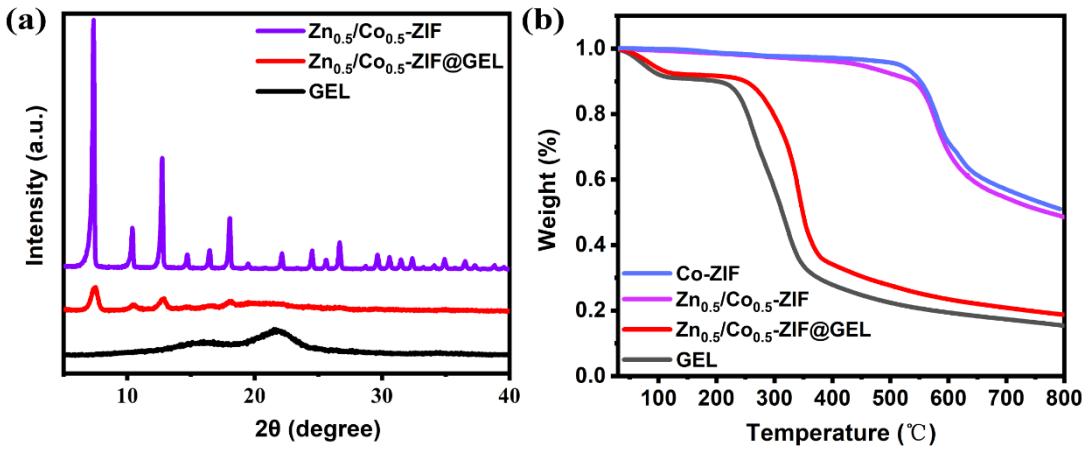

Fig. 4. (a) XRD image of $Zn_{0.5}/Co_{0.5}$-ZIF@GEL, (b) TG image of $Zn_{0.5}/Co_{0.5}$-ZIF@GEL.

The XRD pattern of GEL, $Zn_{0.5}/Co_{0.5}$-ZIF and $Zn_{0.5}/Co_{0.5}$-ZIF@GEL are shown in Fig. 4a. GEL had two weaker and wider diffraction peaks at 12.3 and 20.1°, and could be indexed to the cellulose crystal type II, which is different from the cellulose type I of parent bagasse (Fig. S2), suggesting the successful purification of cellulose for the GEL [45]. The sharp peaks of $Zn_{0.5}/Co_{0.5}$-ZIF were corresponding to the planes of (011), (002), (112) and (222), respectively, which was in accordance with that of the reported Co-ZIF [41]. The $Zn_{0.5}/Co_{0.5}$-ZIF@GEL simultaneously contained the main characteristic peaks of Zn/Co-ZIF and cellulose aerogel, which was further proved the successful combination of $Zn_{0.5}/Co_{0.5}$-ZIF and cellulose aerogel. The characteristic peak of Zn/Co-ZIF was inapparent, which may be because Zn/Co-ZIF was encapsulated in the composite aerogel.

The thermal stability of GEL, $Zn_{0.5}/Co_{0.5}$-ZIF and $Zn_{0.5}/Co_{0.5}$-ZIF@GEL was monitored by TGA, and the results are shown in Fig. 4b. The mass loss of GEL was significant at 250 ~ 380 ℃, and the mass residual rate at 800 ℃ was 14.7%. For $Zn_{0.5}/Co_{0.5}$-ZIF, the mass residue rate reached 42.94% at 800 ℃. The mass residue rate of $Zn_{0.5}/Co_{0.5}$-ZIF@GEL increased to 20% at 800 ℃, indicating that $Zn_{0.5}/Co_{0.5}$-ZIF nanoparticles were successfully immobilized on the bagasse cellulose aerogel matrix, which improved the thermal stability of the composite.

3.3. Chemical element composition of $Zn_{0.5}/Co_{0.5}$-ZIF@GEL

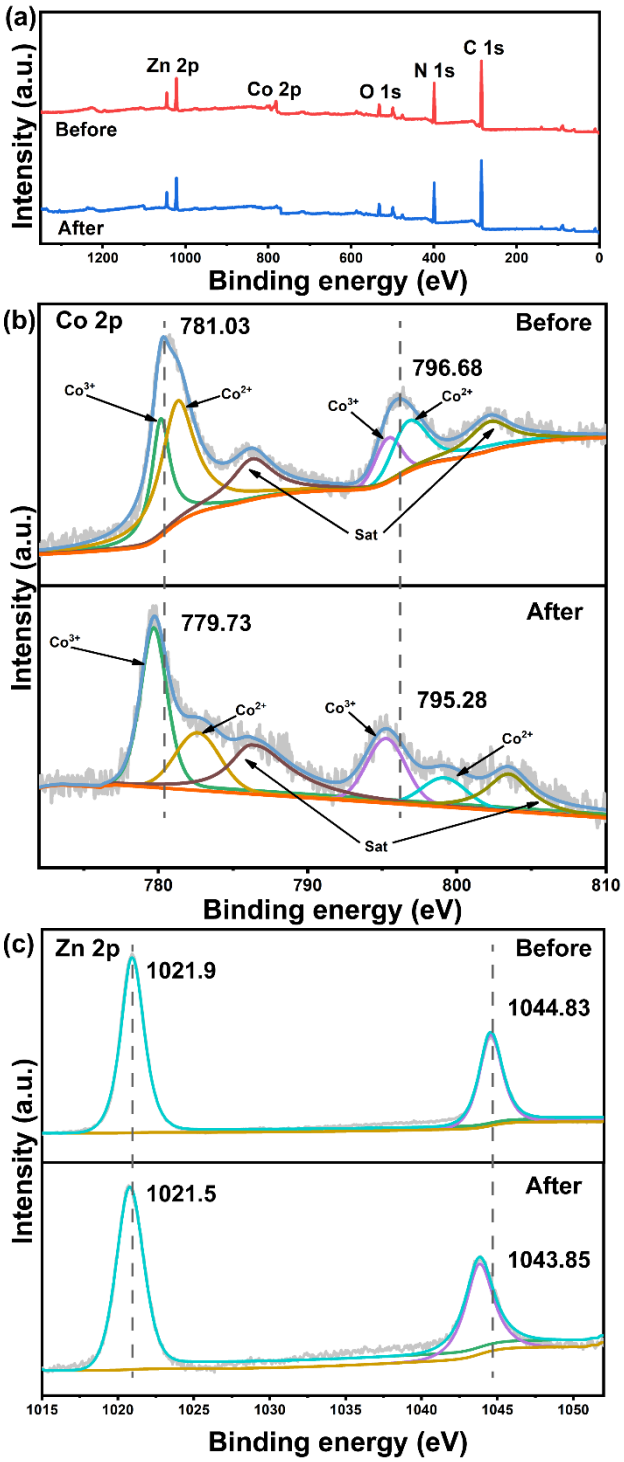

Fig. 5. XPS spectra of $Zn_{0.5}/Co_{0.5}$-ZIF@GEL (a) full-range scan of the samples, (b) Co 2p core level, (c) Zn 2p core level.

In order to further understand the pathway of $Zn_{0.5}/Co_{0.5}$-ZIF@GEL in the PMS activation process, X-ray photoelectron spectroscopy (XPS) was used to determine the

element valence states of the composite aerogel. The change of the chemical valence states of Co and Zn in the XPS reaction provides a possible catalytic way. As shown in Fig. 5a, the survey XPS spectrum displays characteristic peaks of Zn 2p, Co 2p, O 1s, N 1s, and C 1s, indicating the existence of the above elements. There was no obvious change on intensity and binding energy of each element in the spectra before and after use, indicating that Zn/Co-ZIF@GEL has good stability. Fig. 5b shows the XPS spectrum of Co 2p of fresh and used composite aerogels. It can be seen that the two main peaks of Co^{3+} 2p 3/2 and Co^{3+} 2p 1/2 located at 780.2 eV and 794.9 eV, respectively. The other two peaks, 781.9 eV and 796.3 eV, were derived from Co^{2+} 2p 3/2 and Co^{2+} 2p 1/2. And two satellite peaks were accompanied the main peaks at the same time. After the catalytic reaction, the proportion of Co^{2+} dropped from 43.6% to 35.9%, and 23.9% of Co^{3+} was formed, indicating that Co^{2+} and Co^{3+} involved in the PMS activation. It showed that the electron transfer occurred when Co participated in the reaction process. As such, Co^{2+} provided electrons to PMS, then activated PMS to produce $SO_4^{\bullet -}$. At the same time, the valence of Co has also changed from +2 to +3. The reaction formula is as Eq. (1).

Fig. 5c displays the spectrum of Zn 2p, the peak value of Zn 2p before used was at 1021.9 eV. After used, it shifted slightly and moved to 1021.5 eV. And after the catalytic reaction occurred, the peak area was slightly reduced. It showed that part of the Zn^{2+} on the surface of the Zn/Co-ZIF@GEL catalyst has been transformed into Zn^{3+} during the reaction Eq. (2). However, XPS spectrum was not recognized Zn^{3+}. Since it was found that there was no thermodynamically stable Zn^{3+} compound in recent calculations, and Zn^{3+} must be transformed into a stable Zn^{2+} state immediately [46, 47].

$$\equiv Co^{2+} + HSO_5^- \rightarrow \equiv Co^{3+} + SO_4^{\bullet -} + OH^- \quad (1)$$

$$\equiv Zn^{2+} + HSO_5^- \rightarrow \equiv Zn^{3+} + SO_4^{\bullet -} + OH^- \quad (2)$$

It can be inferred that PMS was activated by Co^{2+} and Zn^{2+} on the surface of Zn/Co-ZIF to produce $SO_4^{\bullet -}$. All these findings suggested that Co^{3+} and Zn^{3+} continued to complete the redox cycle, so that the Zn/Co-ZIF@GEL catalyst can work

continuously. And the redox cycles occurred on the surface of Zn/Co-ZIF@GEL made it maintain outstanding catalytic performance [42]. The above reaction formulas are as Eq. (3-4).

$$\equiv Co^{3+} + HSO_5^- \rightarrow \equiv Co^{2+} + SO_4^{\bullet -} + H^+ \quad (3)$$

$$\equiv Zn^{3+} + HSO_5^- \rightarrow \equiv Zn^{2+} + SO_4^{\bullet -} + H^+ \quad (4)$$

3.4. Performance of catalytic degradation by PMS activation

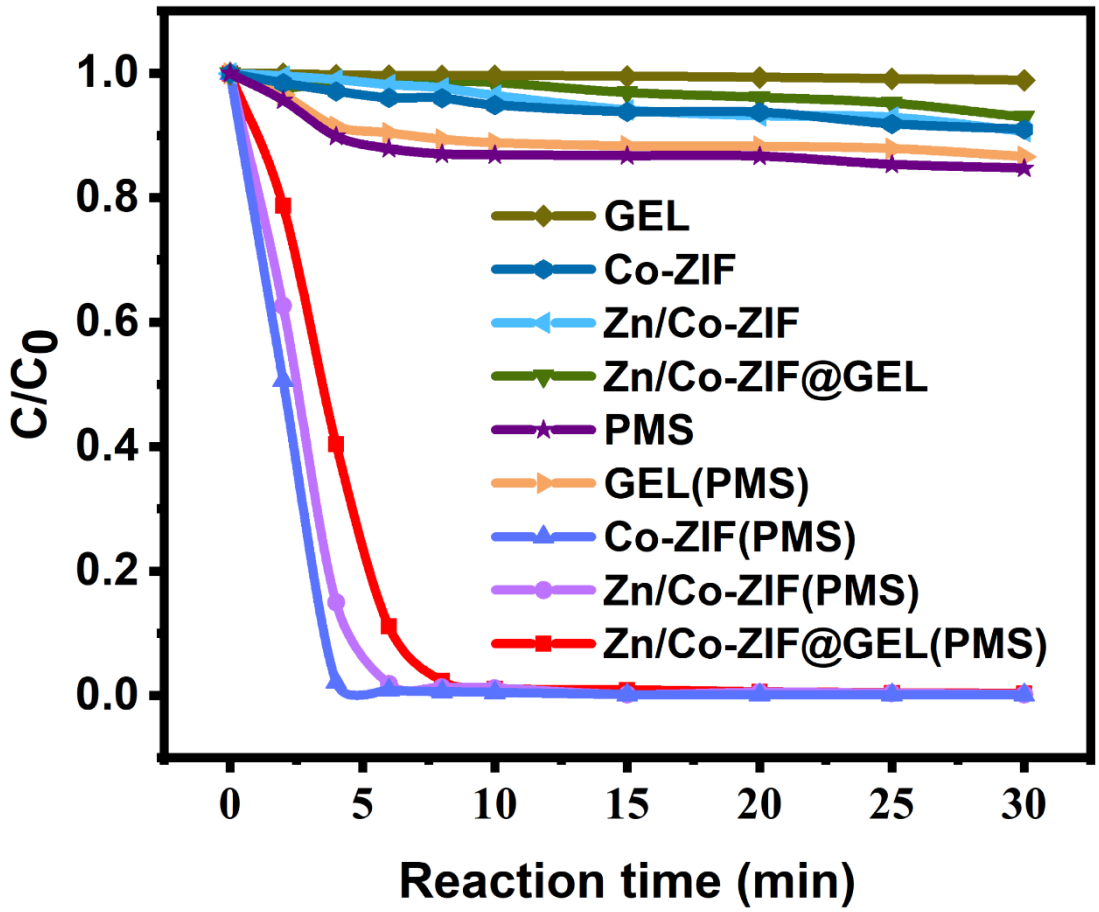

Fig. 6. Degradation performance of GEL, Co-ZIF, $Zn_{0.5}/Co_{0.5}$-ZIF and $Zn_{0.5}/Co_{0.5}$-ZIF@GEL for RhB in PMS system. (experiment conditions: [RhB] = 50 mg/L, [PMS] = 0.4mM, [Co-ZIF] = 50mg/L, [$Zn_{0.5}/Co_{0.5}$-ZIF] = 50mg/L, [$Zn_{0.5}/Co_{0.5}$-ZIF@GEL] = 150 mg/L, pH = 6.8, T = 25 °C)

The catalytic performances of different catalysts were evaluated through PMS activated degradation of cationic dye RhB. Before catalytic reaction, the RhB adsorption performance of GEL, Co-ZIF, $Zn_{0.5}/Co_{0.5}$-ZIF and $Zn_{0.5}/Co_{0.5}$-ZIF@GEL

were investigated without adding PMS. As shown in Fig. 6, negligible removal efficiency of RhB was observed in GEL, which was associated to the macroporous feature and ultralow surface area of GEL (Fig. 3e). In comparison to GEL, Co-ZIF、$Zn_{0.5}/Co_{0.5}$-ZIF and $Zn_{0.5}/Co_{0.5}$-ZIF@GEL showed slightly higher removal amount of RhB (10, 10 and 8%, respectively). However, this results still indicated the limitation of adsorption removal of RhB by using GEL, Co-ZIF, $Zn_{0.5}/Co_{0.5}$-ZIF and $Zn_{0.5}/Co_{0.5}$-ZIF@GEL. Thus, it is necessary to stimulate the catalytic reaction to achieve high removal performance of RhB on as-synthesized catalysts.

PMS was applied to the systems and activated by the catalysts. Degradation experiments of RhB were carried out with PMS alone, GEL with PMS, Co-ZIF with PMS, $Zn_{0.5}/Co_{0.5}$-ZIF with PMS and $Zn_{0.5}/Co_{0.5}$-ZIF@GEL with PMS. As showed in Fig. 6, the degradation curves of PMS alone and GEL with PMS were almost identical, which both have 15% degradation efficiency of RhB. This suggested the limited oxidation activity of PMS without activation and inertness of GEL. Once the as-prepared catalysts applied into the system with PMS, significant enhancement in degradation efficiency of RhB were observed. All catalysts (Co-ZIF, $Zn_{0.5}/Co_{0.5}$-ZIF and $Zn_{0.5}/Co_{0.5}$-ZIF@GEL) with PMS showed similar ultimate degradation efficiency of 100% within 10 min but different kinetic rates of reaction. As depicted in Fig. S3, the kinetic rates of Co-ZIF, $Zn_{0.5}/Co_{0.5}$-ZIF and $Zn_{0.5}/Co_{0.5}$-ZIF@GEL were calculated to be 0.309, 0.066 and 0.059 min^{-1}. The Compared with the degradation rate of $Zn_{0.5}/Co_{0.5}$-ZIF and $Zn_{0.5}/Co_{0.5}$-ZIF@GEL were relative sluggish to Co-ZIF, which was probably the inertness of doping metal of Zn.

3.5. Effect of catalyst dosage, initial pH, PMS concentration and initial RhB concentration on catalytic activity

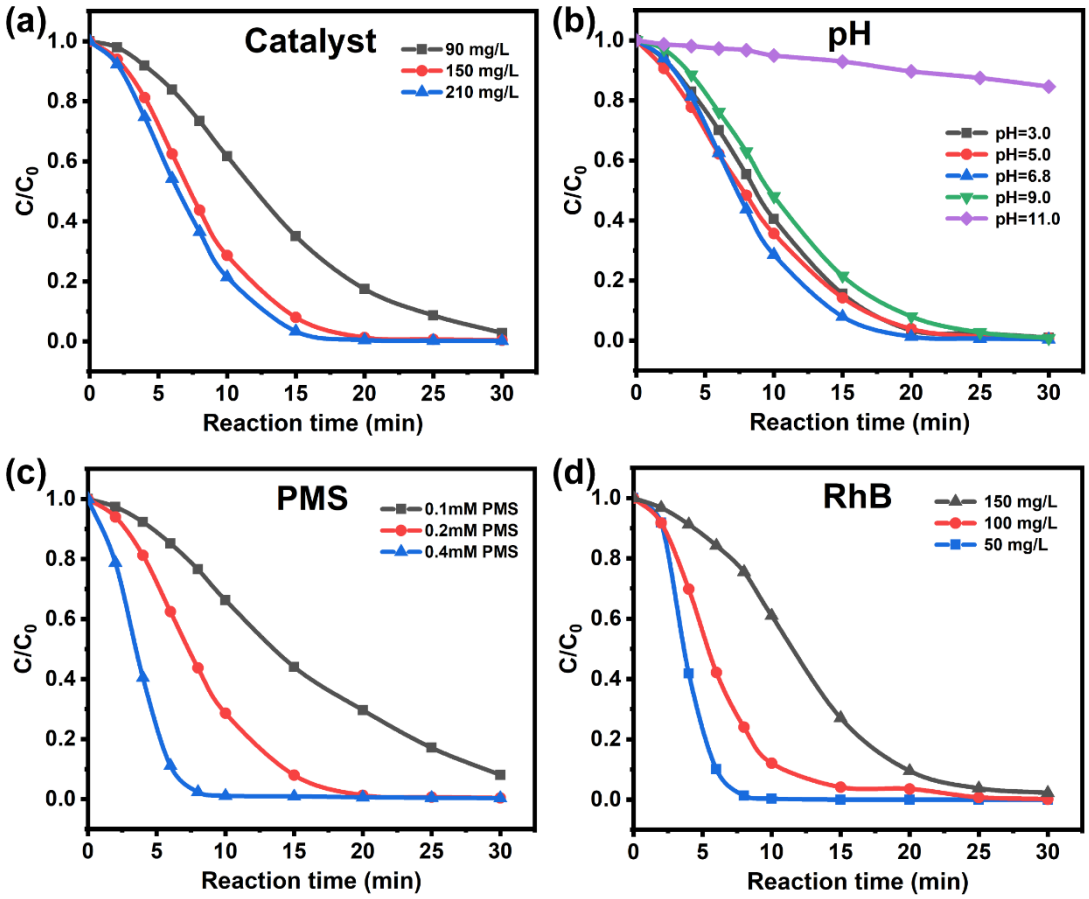

Fig. 7. The effect of different conditions of RhB removal rate: (a) catalyst dosage, (b) initial solution pH, (c) PMS concentration, (d) initial concentration of RhB. (experiment conditions: [RhB] = 50 mg/L (for a, b, c), [PMS] = 0.2 mM (for a, b, d), [catalyst] = 150 mg/L (for b, c, d), pH = 6.8 (for a, c, d), T=25°C).

The effect of operation parameters (catalyst dosage, initial pH, PMS concentration and initial RhB concentration) on the degradation performance of RhB in of $Zn_{0.5}/Co_{0.5}$-ZIF@GEL/PMS was explored and shown in Fig. 7(a-d). The degradation results of RhB using different dosage of catalysts from 90-210 mg/mL were shown in Fig. 7a. The degradation percentage could be achieved to 98% within 30 min for 90 mg/L of $Zn_{0.5}/Co_{0.5}$-ZIF@GEL. As the catalyst dosage added, the significant increase in the degradation efficiency was observed. Compared with the case of catalyst dosage at 90 mg/mL, higher removal percentage (100%) for RhB within shorter time (20 min) was observed in case of catalyst dosage at 150 and 210 mg/mL. This was attributed to the

increase of catalytic activity sites, which is favorable for promoting the activation of PMS and generating higher amounts of radicals. It was noted that the degradation rate increases rapidly when the catalyst dosage increased from 90 to150 mg/mL, but when the catalyst dosage increased from 150 mg/mL to 210 mg/mL, the degradation rate was slow and almost approaching the equilibrium of the catalytic reaction. This indicated that the self-quenching of free radicals may occur at high concentration (Eq. (5) and (6)), thus limiting the increase of the reaction rate [48].

$$SO_4^{\bullet -} + SO_4^{\bullet -} \rightarrow S_2O_8^{2-} \quad (5)$$

$$SO_4^{\bullet -} + OH^{\bullet} \rightarrow HSO_5^{-} \quad (6)$$

Initial pH is one of the critical parameters that could affect the catalytic performance. Fig. 7b depicted the results of RhB degradation in the catalytic systems with different initial pH ranging from 3-11. Obviously, in the wide pH range of 3.0 ~ 9.0, pH had no obvious effect on the degradation effect of RhB, indicated that the Zn/Co-ZIF@GEL/PMS system has good pH resistance. However, when the pH reached 11, the performance decreased significantly, which may be due to the formation of $Co(OH)_2$ with low reactivity on the surface of the catalyst and the conversion of a large amount of $SO_4^{\bullet -}$ to $OH^{\bullet}$. Under alkaline conditions (initial pH = 11), PMS may undergo self-degradation without producing $SO_4^{\bullet -}$, and the following reaction occurs (Eq. (7)-(10)), thereby reducing the degradation ability of RhB.

$$HSO_5^{-} + H_2O \Leftrightarrow SO_5^{2-} + H_3O^{+} \quad (7)$$

$$HSO_5^{-} + SO_5^{2-} \rightarrow HSO_6^{-} + SO_4^{2-} \quad (8)$$

$$HSO_6^{-} + OH^{-} \rightarrow SO_4^{2-} + H_2O + O_2 \quad (9)$$

$$SO_4^{\bullet -} + OH^{-} \rightarrow SO_4^{2-} + OH^{\bullet} \quad (10)$$

The effect of PMS concentration on RhB degradation was shown in Fig. 7c. PMS as the source of $OH^{\bullet}$ and $SO_4^{\bullet -}$ [49], its content has a critical effect on the reaction. The results showed that the PMS concentration from 0.1 mM to 0.4 mM has a significant effect on the catalytic performance. The catalytic performance was not satisfactory when the PMS concentration (0.1mM) was insufficient, which was caused by the rapid

consumption of PMS by $Zn_{0.5}/Co_{0.5}$-ZIF@GEL. ~~When the PMS amount has reached to 0.4mM, the effect of degrading RhB was inhibited. The reason might be once the amount of PMS increase in the solution, the acidity and alkalinity of the solution was destroyed and caused free radical quenching, thereby the activity of catalyst was inhibited [50].~~ When the PMS concentration has reached to 0.4 mM, the effect of degrading RhB has increased significantly. High concentrations of PMS generated more free radicals and provided more active sites for the catalyst. At this point the reaction system achieved the highest reaction rate and the complete degradation rate.

Fig. 7d shows the degradation efficiency of RhB at different initial concentrations, and further investigates the catalytic activity of $Zn_{0.5}/Co_{0.5}$-ZIF@GEL. It clearly found that the initial concentration of 50 mg/L and 100 mg/L initial concentration achieved completely removal within 25 min. Moreover, RhB with high concentrations had a slight decline removal in the same reaction time, 97.6% degradation effect was reached at 150 mg/L in 30 min. This could be attributed to when the concentration of RhB goes up, the concentration difference between RhB and radicals increased, resulting in the slower reaction rate [51].

3.6. Identification of reactive species and activation mechanisms

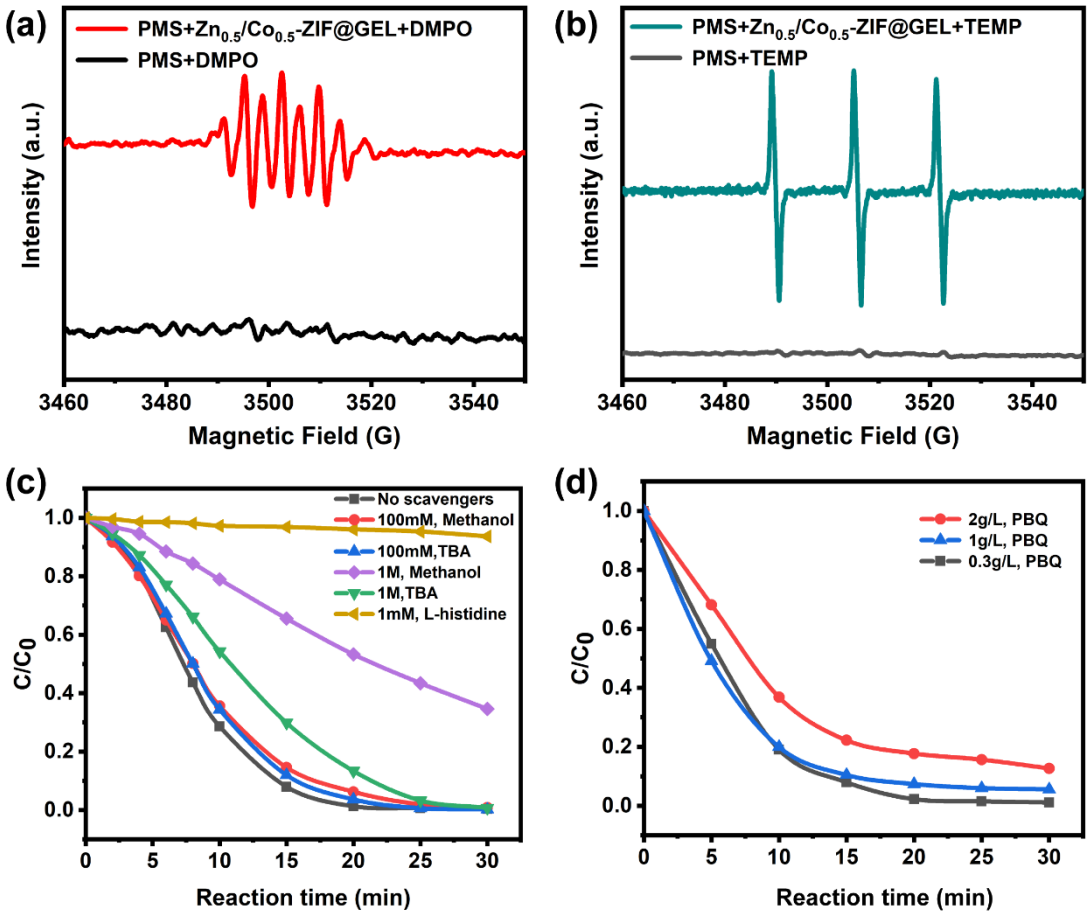

Fig. 8. (a)(b) EPR spectra of DMPO and TEMP as the trapping agent, respectively, (c)(d) Effects of different free radical scavengers on the degradation of RhB in $Zn_{0.5}/Co_{0.5}$-ZIF@GEL/PMS system. (experiment conditions: [RhB] = 50 mg/L, [PMS] = 0.2mM, [catalyst] = 150 mg/L, pH = 6.8, T = 25 °C).

In the process of PMS activation by transition metals, $SO_4^{\bullet -}$ and $OH^{\bullet}$ are simultaneously produced [22]. DMPO was used as the spin-trapping agent for $SO_4^{\bullet -}$ and $OH^{\bullet}$, and EPR spectroscopy of the radical was identified. As shown in Fig. 8a, when PMS was participated in the reaction solution, only a weak signal appeared which was caused by the self-decomposition of PMS in the absence of catalyst. It was worth noting that there were no distinctive signals of DMPO-$SO_4^{\bullet -}$ and DMPO-$OH^{\bullet}$ appear in the Zn/Co-ZIF@GEL system, but clear seven peaks signal ($\alpha N = 7.3 \pm 0.1$ G and $\alpha H = 3.9 \pm 0.1$ G) [48]. The phenomenon was due to the hyperfine splitting of DMPO oxidation

products, which were 5,5-dimethylpyrrolidone-2-(oxy)-(1) or 5,5-dimethyl-2-pyrrolidone-1-oxyl (DMPO-X) [52, 53]. The appearance of DMPO-X meant that highly active oxygen-containing molecules were produced during the activation reaction of PMS, which leads to the rapid oxidation of DMPO [54]. The generated oxidized molecules had strong oxidizing ability and were difficult to capture by adding DMPO. On the one hand, the disproportionation reaction of superoxide radicals in water may inhibit the reaction between superoxide radicals and DMPO. On the other hand, it may be that the DMPO-$O_2^{\bullet-}$ signal was easily covered by the DMPO-X signal. And similar phenomenon has been seen in previous studies[55, 56].

In order to identify other free radicals that may form, TEMP was used as the spin-trapping agent for testing. As shown in Fig. 8b, it can be observed that PMS/TEMP can form a weak triplet signal with an intensity ratio of 1:1:1, which may be caused by the self-degradation of PMS to form $^1O_2$ (Eq. (11)) [57]. However, in the $Zn_{0.5}/Co_{0.5}$-ZIF @GEL/PMS system, the triplet high-intensity EPR spectral peak (αN = 16.9 g) was observed, which was consistent with the TEMP-singlet oxygen $^1O_2$ adduct (TEMP) [58], which indicated that Zn/Co-ZIF can promote the self-degradation of PMS and produce singlet oxygen. And it proved that $^1O_2$ played indispensable role in degradation process of Zn/Co-ZIF/PMS system. It can be recommended that the non-radical pathway ($^1O_2$) and free radicals ($SO_4^{\bullet-}$, $OH^{\bullet}$ and $O_2^{\bullet-}$) jointly act on the degradation of RhB.

$$HSO_5^- + SO_5^{2-} \rightarrow HSO_4^- + SO_4^{2-} + {}^1O_2 \quad (11)$$

In order to further understand the degradation mechanism, the results of using methanol, *tert*-butyl alcohol (TBA) and L-histidine as free radical scavengers are shown in Fig. 8c. Methanol was regarded as a scavenger of sulfate radical ($SO_4^{\bullet-}$) and hydroxyl radical ($OH^{\bullet}$), TBA was a selective probe for $OH^{\bullet}$, and benzoquinone (PBQ) was used as a scavenger of $O_2^{\bullet-}$, L-Histidine acted as a scavenger of singlet oxygen ($^1O_2$) [59].

When there was no scavenger, the removal efficiency of 98.7% can be achieved after 20 min of reaction. When equal amounts (100 mM) of TBA and methanol were added, the degradation of RhB was only slightly inhibited. After adding 1M TBA and methanol, both of them showed more obvious inhibition effect, but the inhibition effect of methanol was more significant than that of TBA, and the degradation effect could

reach 65.4%. The phenomenon can be attributed to the fact that both $OH^{\bullet}$ and $SO_4^{\bullet -}$ were produced and participate in the degradation of RhB, but $SO_4^{\bullet -}$ played a more important role than $OH^{\bullet}$. But this meant that there were some other common free radicals or non-radical reactive molecules involved in the reaction. The result of adding PBQ into the solution is shown in Fig. 8d. When different amount of PBQ was added (0.3 g/L, 1 g/L, and 2 g/L), the degradation effect of RHB decreased from 98.8% to 94.4 %, 87.27 %, respectively. Therefore, we inferred that a small amount of $O_2^{\bullet -}$ was produced by the oxidation of Co^{2+} and Zn^{2+} by O_2 in the reaction process (Eq. (12) and (13)) [50], but $O_2^{\bullet -}$ had limited degradation of RhB. Since $^1O_2$ was regarded as a typical active oxidation molecule (ROS) in non-free radical processes [60], we speculated that $^1O_2$ may exist in the reaction system of Zn/Co-ZIF@GEL/PMS. Therefore, when 1 mM L-histidine was added into the reaction solution (Fig. 8c), the degradation of RhB by Zn/Co-ZIF@GEL/PMS system was significantly inhibited, and only 9.9% of RhB was removed. It indicated that the non-radical ($^1O_2$) degradation route was the main degradation route of RhB. In combination with the previous results, it can be determined that in the Zn/Co-ZIF@GEL/PMS system, the non-free radical pathway ($^1O_2$) and free radicals ($SO_4^{\bullet -}$, $OH^{\bullet}$ and $O_2^{\bullet -}$) interacted together to achieve the degradation effect of RhB.

$$Co^{2+} + O_2 \rightarrow Co^{3+} + O_2^{\bullet -} \quad (12)$$

$$Zn^{2+} + O_2 \rightarrow Zn^{3+} + O_2^{\bullet -} \quad (13)$$

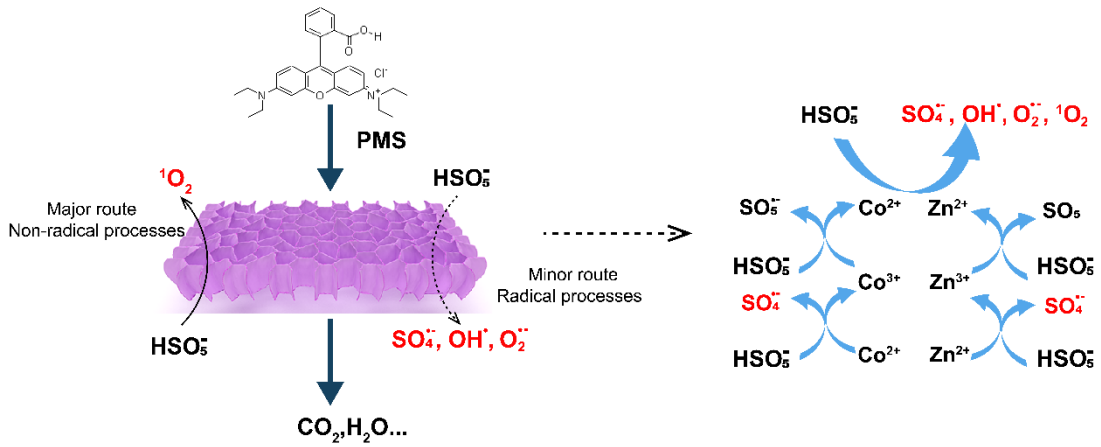

Fig. 9. The degradation mechanisms of RhB in Zn/Co-ZIF@GEL/PMS system.

In summary, based on the above results and previous studies, a possible mechanism for the efficient activation of PMS by Zn/Co-ZIF@GEL was proposed (Fig. 9). First, the HSO_5^- in PMS could be activated by Co^{2+} and Zn^{2+} ions in Zn/Co-ZIF@GEL, electron transfer occurred to produce $SO_4^{\bullet -}$, and the valence of Co and Zn also converted +2 into +3 (Eq. (1) and (2)). Moreover, Co^{3+} and Zn^{3+} continue to react with HSO_5^- to produce Co^{2+} and Zn^{2+} when the reaction goes on (Eq. (3) and (4)), so that the effective redox cycle was maintained. Also, $O_2^{\bullet -}$ and $OH^{\bullet}$ were generated during this process, which could contribute to the degradation of RhB (Eq. (12-15)). In addition, we have confirmed that the non-radical degradation mechanism of Zn-Co/ZIF@GEL/PMS system was dominated by $^1O_2$ which produced by self-degradation of PMS (Eq. 11). Besides, aerogel had a large specific surface area and high porosity, which was conducive to the retention of RhB molecules, so as to make the degradation of pollutants more efficient.

$$SO_4^{\bullet -} + H_2O \rightarrow OH^{\bullet} + H^+ + SO_4^{2-} \quad (14)$$

$$SO_4^{\bullet -} + OH^- \rightarrow OH^{\bullet} + SO_4^{2-} \quad (15)$$

3.7. Structural and composition stability of $Zn_{0.5}/Co_{0.5}$-ZIF@GEL under PMS activation catalysis

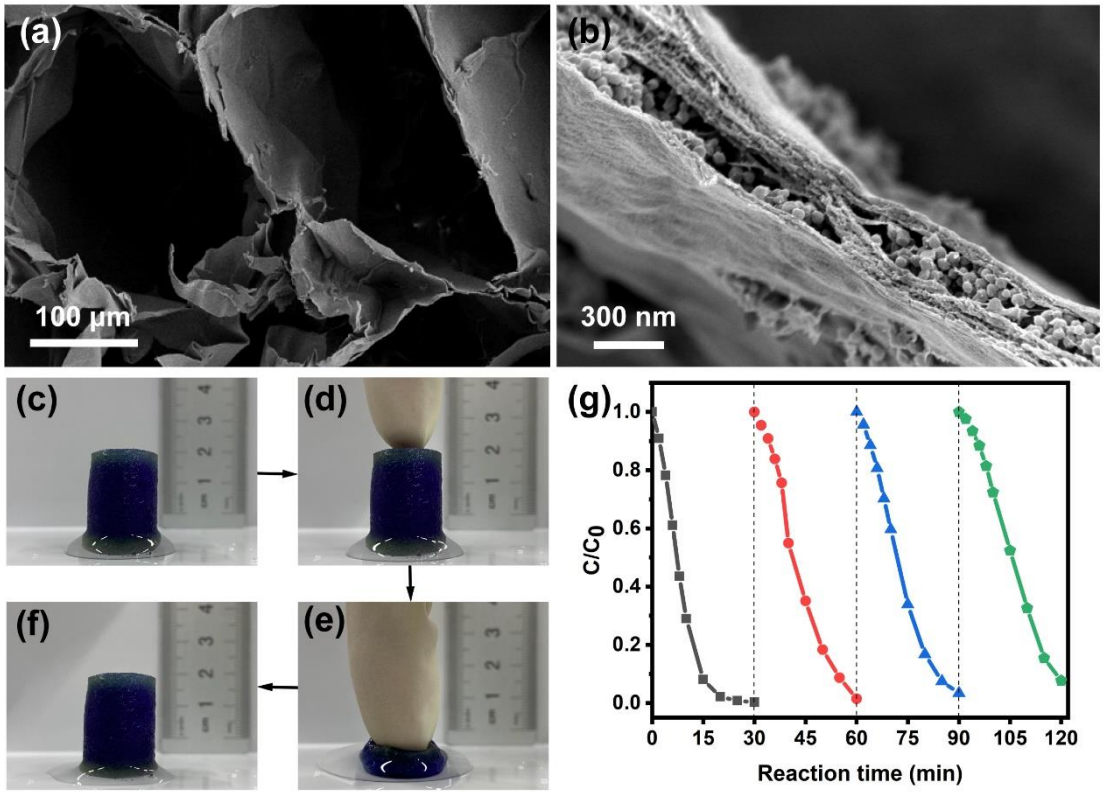

Fig. 10. (a)(b) SEM image of $Zn_{0.5}/Co_{0.5}$-ZIF@GEL after 4 cycles, (c-f) The process of restoring the water-containing composite aerogel to its original state after being compressed, (g) Recycling ability for RhB removal by $Zn_{0.5}/Co_{0.5}$-ZIF@GEL.

$Zn_{0.5}/Co_{0.5}$-ZIF@GEL had demonstrated its high efficiency as a heterogeneous catalyst to activate PMS, but for the long-term use of catalyst, the evaluation of its recyclability was necessary. In order to investigate the reusability and stability of $Zn_{0.5}/Co_{0.5}$-ZIF@GEL in PMS activation, four consecutive parallel degradation experiments of RhB were carried out under the same reaction conditions. Fig. 10a and b are SEM images after four cycles of Zn/Co-ZIF@GEL. It can be seen that bagasse cellulose composite aerogel still maintained the porous structure and the aerogel skeleton was not damaged. With the increase of the number of cycles, the microstructure of the Zn/Co-ZIF nanoparticles contained in the pore wall of cellulose was not destroyed, and a large amount of Zn/Co-ZIF was still retained in the pore wall, which could be reused continuously. Zn/Co-ZIF nanoparticles were encapsulated in

aerogel matrix and this type of encapsulation structure will minimize the shedding of nanoparticles during use. The elemental mapping with before and after using Zn/Co-ZIF@GEL demonstrated that Co and Zn were uniformly distributed in the composite aerogel before and after use (Fig. S4).

The influence of PMS concentration on the dissolution of cobalt ions in Co-ZIF, $Zn_{0.5}/Co_{0.5}$-ZIF and $Zn_{0.5}/Co_{0.5}$-ZIF@GEL is shown in Fig. S5. At different additions of PMS concentrations, the cobalt ions dissolution of Zn/Co-ZIF@GEL was much lower than that of Co-ZIF and Zn/Co-ZIF. The content of Co loaded on the composite aerogel was approximately 4.6 wt%. Compared to the dissolved content of Co, ~~This indicated that~~ bagasse cellulose aerogel had a good protective effect on cobalt ions in the reaction system. In addition, the dissolution amounts of cobalt ions of Co-ZIF in different PMS concentrations was about three times that of Zn/Co-ZIF. Implying that the addition of Zn^{2+} can effectively improve the chemical stability of ZIFs and reduce the dissolution amount of Co^{2+}, so as to ensure the long-term stable use of Zn/Co-ZIF@GEL catalyst. In addition, when the PMS concentration was 0.4 mM, the cobalt ions were all dissolved more than 1 mg/L. This was because with the increase of PMS concentration, the pH in the reaction system continued to decrease, led to a decrease in the stability of Zn/Co-ZIF. At the same time, the free radicals produced by catalyzing PMS will also cause a certain amount of damage to Zn/Co-ZIF and Zn/Co-ZIF@GEL, leading to an increase in the dissolution of cobalt ions.

3.8. Reusability of Zn/Co-ZIF@GEL

Fig. 10(c-f) are the process of the water-containing composite aerogel returning to its original state after being completely compressed. First, pressure applied to the water-containing composite aerogel to make it completely compressed, and the water adsorbed in the composite aerogel was extruded. The pressure then removed and the composite aerogel began to absorb water and fully returned to its original shape. ~~However,~~ It indicated that the composite aerogel can be easily removed from water and reused without changing the aerogel morphology, which indicated that the composite aerogel has good reusability.

Catalyst with good stability and reusability were strongly expected in practical application. Therefore, catalytic recycling measurements of $Zn_{0.5}/Co_{0.5}$-ZIF@GEL were conducted and the results were showed in Fig. 10g. After four-cycle test, the catalytic degradation efficiency for RhB in $Zn_{0.5}/Co_{0.5}$-ZIF@GEL/PMS system slightly decreased but maintained high reusability. The slight decrease of catalytic efficiency might be due to the influence of the change of active site and surface coverage on the intermediates produced during the reaction, but the $Zn_{0.5}/Co_{0.5}$-ZIF@GEL after the reaction still has a high electron transfer efficiency so that has a good reusability [61].

3.9. The role of aerogel in reaction system

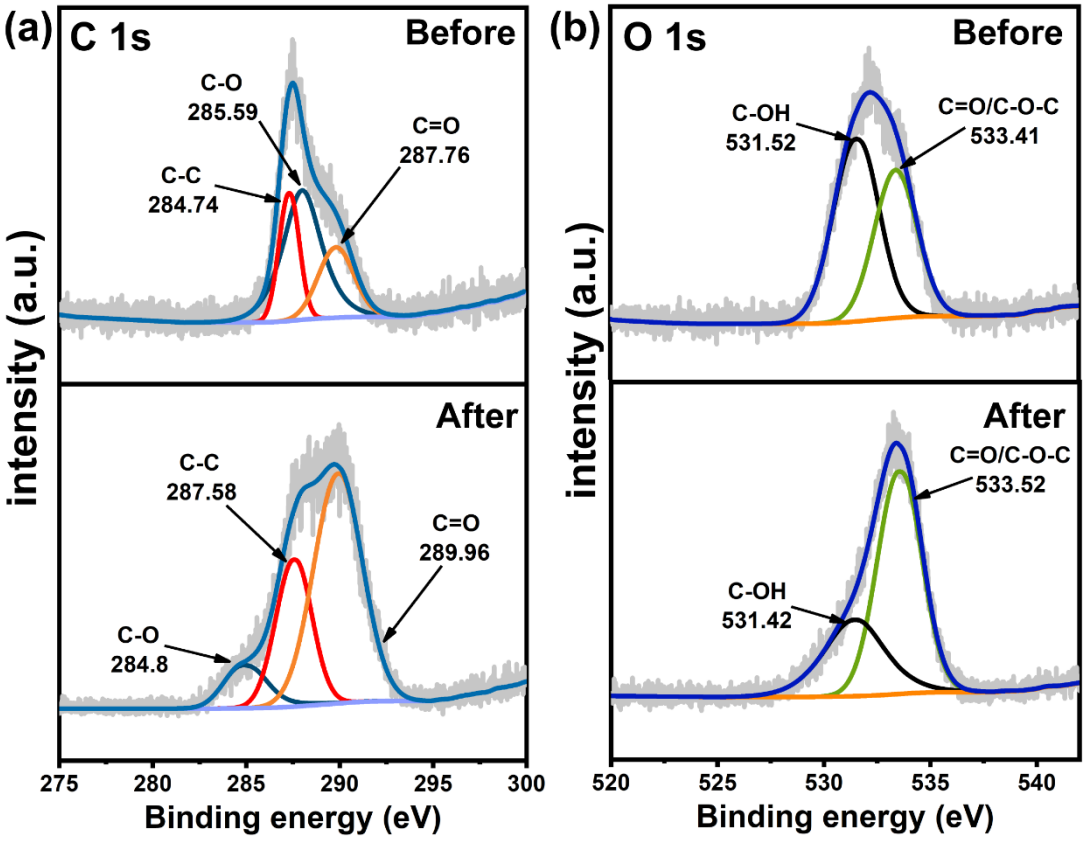

Fig. 11. XPS spectra of $Zn_{0.5}/Co_{0.5}$-ZIF@GEL (a) C 1s core level, (b) O 1s core level.

In order to detect the role of aerogel in the activation of PMS, XPS was further used to study the reaction process of composite aerogel. Fig. 11 shows the core level XPS spectra for C 1s and O 1s. In the C1s spectrum of fresh Zn/Co-ZIF@GEL (Fig. 11a), the peaks at 284.74 eV, 285.59 eV and 287.76 eV belonged to C-C, C-O and C=O,

respectively, which were mainly derived from cellulose. Compared with fresh C 1s, the proportion of C=O increased from 21.9% to 46.9%, C-C was shifted from 284.74 eV to 287.58 eV, C-O dropped from 39.8% to 16.4% after PMS activation. This indicated that some of C-O on the aerogel surface were reduced to C=O, which could be attributed to the interaction with Zn/Co-ZIF@GEL and PMS [62, 63]. As shown in Fig. 11b, for the unused XPS spectrum of O 1s, the binding energy of C-OH appeared at 531.52eV, and the peak of C=O/C-O-C was at 533.41 eV. It can be observed that after the reaction, the ratio of C=O/C-O-C increased from 42.1% to 69%, while the ratio of C-OH decreased by 26.9%. This indicated that oxygen actively participated in the catalytic oxidation reaction which means C-OH might interact with PMS during the degradation process, and the increase of C=O/C-O-C proved that cellulose aerogel was involved in the process of protecting Zn/Co-ZIF [64]. The changes in the strength and binding energy of elements before and after the reaction indicated that the aerogel was involved in the activation of PMS, and the surface of the aerogel was oxidized to produce a large amount of strong oxidizing substances, which further participate in the reaction. This was also the reason why aerogel wrapped Zn/Co-ZIF without affecting its degradation efficiency.

4. Conclusion

In this study, Zn/Co-ZIF@GEL was successfully prepared by doping method as a novel and heterogeneous catalyst, the effect of Zn/Co-ZIF@GEL activated PMS for the removal RhB was studied systematically. Different reaction conditions were applied to degrade RhB and Zn/Co-ZIF@GEL/PMS system exhibited an excellent degradation performance. Almost all RhB (50 mg/L) was degraded in a short time (10 min) and a wide range of pH (3-9). Aerogel was successfully converted from sugarcane bagasse and used as catalyst support, which could effectively reduce the leaching of cobalt ions so that avoid secondary pollution. It was found that Zn doping Co-ZIF showed excellent water stability, the reduction of Co content was not affected degradation performance of ZIFs. In addition, radical-quenching tests and EPR measurements manifest that non-radical pathway play a major role for RhB degradation, radical pathways were minor

pathways. Moreover, based on the cycle tests, Zn/Co-ZIF@GEL remains good stability with 92.3% RhB removal rate after four successive cycles of reaction. The results illustrated that the as-prepared catalyst performed excellent PMS activation and maintained its stability and reaction activity for a long time in the reaction solution. As a harmless and efficient organic pollutant treatment process, Zn/Co-ZIF@GEL provided new insights for the application of new green aerogels in wastewater treatment.

References:

1. Otoni, C.G., et al., *The Food-Materials Nexus: Next Generation Bioplastics and Advanced Materials from Agri-Food Residues.* Adv Mater, 2021: p. e2102520.
2. Qian, Y., F. Zhang, and H. Pang, *A Review of MOFs and Their Composites-Based Photocatalysts: Synthesis and Applications.* Advanced Functional Materials, 2021. **31**(37).
3. Thai, Q.B., et al., *Cellulose-based aerogels from sugarcane bagasse for oil spill-cleaning and heat insulation applications.* Carbohydr Polym, 2020. **228**: p. 115365.
4. Teixeira, S.R., et al., *Valorization of sugarcane bagasse ash: producing glass-ceramic materials.* J Environ Manage, 2014. **134**: p. 15-9.
5. Noor ul, A., et al., *Synthesis and characterization of geopolymer from bagasse bottom ash, waste of sugar industries and naturally available china clay.* Journal of Cleaner Production, 2016. **129**: p. 491-495.
6. Teixeira, S.R., et al., *Sugarcane Bagasse Ash as a Potential Quartz Replacement in Red Ceramic.* Journal of the American Ceramic Society, 2008. **91**(6): p. 1883-1887.
7. Patcharin, W., K. Sriamporn, and A. Kanokkan, *Utilization Biomass from Bagasse Ash for Phillipsite Zeolite Synthesis.* Advanced Materials Research, 2011. **383-390**: p. 4038-4042.
8. Xu, Q., et al., *Characteristics and Applications of Sugar Cane Bagasse Ash Waste in Cementitious Materials.* Materials (Basel), 2018. **12**(1).
9. Peiris, C., et al., *Biochar based removal of antibiotic sulfonamides and tetracyclines in aquatic environments: A critical review.* Bioresour Technol, 2017. **246**: p. 150-159.
10. Zhu, H., Q. Zhang, and S. Zhu, *Alginate Hydrogel: A Shapeable and Versatile Platform for in Situ Preparation of Metal-Organic Framework-Polymer Composites.* ACS Appl Mater Interfaces, 2016. **8**(27): p. 17395-401.
11. Yang, W., et al., *Shapeable three-dimensional CMC aerogels decorated with Ni/Co-MOF for rapid and highly efficient tetracycline hydrochloride removal.* Chemical Engineering Journal, 2019. **375**.
12. Moon, R.J., et al., *Cellulose nanomaterials review: structure, properties and nanocomposites.* Chem Soc Rev, 2011. **40**(7): p. 3941-94.
13. Zhu, H., et al., *Flexible and Porous Nanocellulose Aerogels with High Loadings of Metal-Organic-Framework Particles for Separations Applications.* Adv

Mater, 2016. **28**(35): p. 7652-7.
14. Liu, C., et al., *Novel carbon based Fe-Co oxides derived from Prussian blue analogues activating peroxymonosulfate: Refractory drugs degradation without metal leaching.* Chemical Engineering Journal, 2020. **379**.
15. Xin, S., et al., *High efficiency heterogeneous Fenton-like catalyst biochar modified CuFeO2 for the degradation of tetracycline: Economical synthesis, catalytic performance and mechanism.* Applied Catalysis B: Environmental, 2021. **280**.
16. Li, Y., et al., *Trace pyrolyzed ZIF-67 loaded activated carbon pellets for enhanced adsorption and catalytic degradation of Rhodamine B in water.* Chemical Engineering Journal, 2019. **375**.
17. Chi, H., et al., *Ferrous metal-organic frameworks with stronger coordinatively unsaturated metal sites for persulfate activation to effectively degrade dibutyl phthalate in wastewater.* J Hazard Mater, 2019. **377**: p. 163-171.
18. Li, J., et al., *Enhancement of the degradation of atrazine through CoFe2O4 activated peroxymonosulfate (PMS) process: Kinetic, degradation intermediates, and toxicity evaluation.* Chemical Engineering Journal, 2018. **348**: p. 1012-1024.
19. Li, C., et al., *Tunable titanium metal–organic frameworks with infinite 1D Ti–O rods for efficient visible-light-driven photocatalytic H2 evolution.* Journal of Materials Chemistry A, 2019. **7**(19): p. 11928-11933.
20. Zhou, C., et al., *Strategies for enhancing the perylene diimide photocatalytic degradation activity: method, effect factor, and mechanism.* Environmental Science: Nano, 2021. **8**(3): p. 602-618.
21. He, C., et al., *Rational design to manganese and oxygen co-doped polymeric carbon nitride for efficient nonradical activation of peroxymonosulfate and the mechanism insight.* Chemical Engineering Journal, 2022. **430**.
22. Ghanbari, F. and M. Moradi, *Application of peroxymonosulfate and its activation methods for degradation of environmental organic pollutants: Review.* Chemical Engineering Journal, 2017. **310**: p. 41-62.
23. Lin, K.-Y.A. and H.-A. Chang, *Zeolitic Imidazole Framework-67 (ZIF-67) as a heterogeneous catalyst to activate peroxymonosulfate for degradation of Rhodamine B in water.* Journal of the Taiwan Institute of Chemical Engineers, 2015. **53**: p. 40-45.
24. Hu, P. and M. Long, *Cobalt-catalyzed sulfate radical-based advanced oxidation: A review on heterogeneous catalysts and applications.* Applied Catalysis B: Environmental, 2016. **181**: p. 103-117.
25. Howarth, A.J., et al., *Chemical, thermal and mechanical stabilities of metal–organic frameworks.* Nature Reviews Materials, 2016. **1**(3).
26. Fang, C., et al., *Co–Ferrocene MOF/Glucose Oxidase as Cascade Nanozyme for Effective Tumor Therapy.* Advanced Functional Materials, 2020. **30**(16).
27. Hwang, J., et al., *Controlling the morphology of metal-organic frameworks and porous carbon materials: metal oxides as primary architecture-directing agents.* Chem Soc Rev, 2020. **49**(11): p. 3348-3422.

28. Sun, L., M.G. Campbell, and M. Dinca, *Electrically Conductive Porous Metal-Organic Frameworks.* Angew Chem Int Ed Engl, 2016. **55**(11): p. 3566-79.
29. Ding, M., X. Cai, and H.L. Jiang, *Improving MOF stability: approaches and applications.* Chem Sci, 2019. **10**(44): p. 10209-10230.
30. Jhung, S.H., et al., *Microwave Synthesis of Chromium Terephthalate MIL-101 and Its Benzene Sorption Ability.* Advanced Materials, 2007. **19**(1): p. 121-124.
31. Wang, Q. and D. Astruc, *State of the Art and Prospects in Metal-Organic Framework (MOF)-Based and MOF-Derived Nanocatalysis.* Chem Rev, 2020. **120**(2): p. 1438-1511.
32. Burtch, N.C., H. Jasuja, and K.S. Walton, *Water stability and adsorption in metal-organic frameworks.* Chem Rev, 2014. **114**(20): p. 10575-612.
33. Gu, A., et al., *The preparation of Ag/ZIF-8@ZIF-67 core-shell composites as excellent catalyst for degradation of the nitroaromatic compounds.* Applied Surface Science, 2020. **516**.
34. Chen, B., et al., *Zeolitic imidazolate framework materials: recent progress in synthesis and applications.* J. Mater. Chem. A, 2014. **2**(40): p. 16811-16831.
35. Liu, Y., et al., *Activation of persulfate with metal–organic framework-derived nitrogen-doped porous Co@C nanoboxes for highly efficient p-Chloroaniline removal.* Chemical Engineering Journal, 2019. **358**: p. 408-418.
36. Zhong, G., D. Liu, and J. Zhang, *The application of ZIF-67 and its derivatives: adsorption, separation, electrochemistry and catalysts.* Journal of Materials Chemistry A, 2018. **6**(5): p. 1887-1899.
37. Ma, W., et al., *Nitrogen, phosphorus, and sulfur tri-doped hollow carbon shells derived from ZIF-67@poly (cyclotriphosphazene-co-4, 4'-sulfonyldiphenol) as a robust catalyst of peroxymonosulfate activation for degradation of bisphenol A.* Carbon, 2018. **137**: p. 291-303.
38. Wang, C., et al., *Applications of water stable metal-organic frameworks.* Chem Soc Rev, 2016. **45**(18): p. 5107-34.
39. Ren, W., et al., *Recyclable metal-organic framework/cellulose aerogels for activating peroxymonosulfate to degrade organic pollutants.* Chemical Engineering Journal, 2018. **349**: p. 766-774.
40. Chen, Y.Z., et al., *From Bimetallic Metal-Organic Framework to Porous Carbon: High Surface Area and Multicomponent Active Dopants for Excellent Electrocatalysis.* Adv Mater, 2015. **27**(34): p. 5010-6.
41. Zhou, K., et al., *Characterization and properties of Zn/Co zeolitic imidazolate frameworks vs. ZIF-8 and ZIF-67.* Journal of Materials Chemistry A, 2017. **5**(3): p. 952-957.
42. Butova, V.V., et al., *Zn/Co ZIF family: MW synthesis, characterization and stability upon halogen sorption.* Polyhedron, 2018. **154**: p. 457-464.
43. Taheri, M., T.G. Enge, and T. Tsuzuki, *Water stability of cobalt doped ZIF-8: a quantitative study using optical analyses.* Materials Today Chemistry, 2020. **16**.
44. Li, H., et al., *Enhanced hydrostability in Ni-doped MOF-5.* Inorg Chem, 2012. **51**(17): p. 9200-7.
45. Wang, H., et al., *Preparation of tough cellulose II nanofibers with high thermal*

stability from wood. Cellulose, 2014. **21**(3): p. 1505-1515.
46. Schlöder, T., M. Kaupp, and S.J.J.o.t.A.C.S. Riedel, *Can zinc really exist in its oxidation state+ III?* 2012. **134**(29): p. 11977-11979.
47. Lin, H., et al., *Degradation of bisphenol A by activating peroxymonosulfate with Mn0.6Zn0.4Fe2O4 fabricated from spent Zn-Mn alkaline batteries.* Chemical Engineering Journal, 2019. **364**: p. 541-551.
48. Wu, Z., et al., *Core-shell magnetic Fe3O4@Zn/Co-ZIFs to activate peroxymonosulfate for highly efficient degradation of carbamazepine.* Applied Catalysis B: Environmental, 2020. **277**.
49. !!! INVALID CITATION !!! .
50. Luo, H., et al., *WS2 as highly active co-catalyst for the regeneration of Fe(II) in the advanced oxidation processes.* Chemosphere, 2021. **262**: p. 128067.
51. Zhang, M., et al., *Metal–organic framework derived Co3O4/C@SiO2 yolk–shell nanoreactors with enhanced catalytic performance.* Journal of Materials Chemistry A, 2018. **6**(24): p. 11226-11235.
52. Ma, W., et al., *Non-radical-dominated catalytic degradation of bisphenol A by ZIF-67 derived nitrogen-doped carbon nanotubes frameworks in the presence of peroxymonosulfate.* Chemical Engineering Journal, 2018. **336**: p. 721-731.
53. Fontmorin, J.M., et al., *Stability of 5,5-dimethyl-1-pyrroline-N-oxide as a spin-trap for quantification of hydroxyl radicals in processes based on Fenton reaction.* Water Res, 2016. **99**: p. 24-32.
54. Zhang, M., et al., *Confined pyrolysis of metal–organic frameworks to N-doped hierarchical carbon for non-radical dominated advanced oxidation processes.* Journal of Materials Chemistry A, 2019. **7**(20): p. 12547-12555.
55. Qi, C., et al., *Activation of peroxymonosulfate by base: Implications for the degradation of organic pollutants.* Chemosphere, 2016. **151**: p. 280-8.
56. Li, X., et al., *Single Cobalt Atoms Anchored on Porous N-Doped Graphene with Dual Reaction Sites for Efficient Fenton-like Catalysis.* J Am Chem Soc, 2018. **140**(39): p. 12469-12475.
57. Su, W., et al., *Visible light photocatalysis on praseodymium(III)-nitrate-modified TiO2 prepared by an ultrasound method.* Applied Catalysis B: Environmental, 2008. **77**(3-4): p. 264-271.
58. Chen, C., et al., *Mn3O4 nanodots loaded g-C3N4 nanosheets for catalytic membrane degradation of organic contaminants.* J Hazard Mater, 2020. **390**: p. 122146.
59. Di, J., et al., *Electrochemical activation combined with advanced oxidation on NiCo2O4 nanoarray electrode for decomposition of Rhodamine B.* Journal of Water Process Engineering, 2020. **37**.
60. Sun, H., et al., *Activation of peroxymonosulfate by nitrogen-functionalized sludge carbon for efficient degradation of organic pollutants in water.* Bioresour Technol, 2017. **241**: p. 244-251.
61. Ding, M., et al., *Synergistic Features of Superoxide Molecule Anchoring and Charge Transfer on Two-Dimensional Ti3C2Tx MXene for Efficient Peroxymonosulfate Activation.* ACS Appl Mater Interfaces, 2020. **12**(8): p.

9209-9218.
62. Wang, Y., et al., *Activation of peroxymonosulfate by carbonaceous oxygen groups: experimental and density functional theory calculations.* Applied Catalysis B: Environmental, 2016. **198**: p. 295-302.
63. Li, Z., et al., *Biochar-supported nanoscale zero-valent iron as an efficient catalyst for organic degradation in groundwater.* J Hazard Mater, 2020. **383**: p. 121240.
64. Li, Z., et al., *Converting untreated waste office paper and chitosan into aerogel adsorbent for the removal of heavy metal ions.* Carbohydr Polym, 2018. **193**: p. 221-227.